

GSMMC 2023: FIRE RISK

JAVIER ALMONACID, PAU BATLLE, CLAIRE CHANG, JAMIREE HARRISON, KIMBERLY MATSUDA, LI MENG,
OLIVIA POMERENK, ARNAB ROY, AND RILEY SUPPLE

MENTOR: MANUCHEHR AMINIAN, CAL POLY POMONA

ABSTRACT. On December 30, 2021, the Marshall Fire severely impacted Boulder County, Colorado, costing more than 2 billion USD in damages. According to official reports, several conditions impacted the rapid spread of the fire: dry and warm weather over the previous months, and strong wind currents coming from the nearby mountains. In this report, we survey different risk factors for wildfire spreading into cities and urban areas from mathematical modeling and data analysis perspectives, with the end goal of identifying potential risk of similar events for regions across the United States.

CONTENTS

1. Background	1
2. Data Analysis and Modeling	2
2.1. Data Description and Correlation Analysis	2
2.2. K-Means Clustering	4
2.3. Dynamic Mode Decomposition Using Historical Fire Data	4
3. Shallow-water Approximations for Modeling Wind Flow over Irregular Topography	7
3.1. Introduction: Shallow-water Equations	7
3.2. Numerical method	9
3.3. Predictions arising from shallow-water analysis using elevation data	10
4. Potential Flow to model flow over an obstacle.	11
5. Finite element/volume approaches to modeling flow	12
5.1. A finite element approach	12
5.2. FiPy Simulations	15
6. Conclusions and Future Directions	17
References	17

1. BACKGROUND

Our problem is motivated by insurance companies concerned by catastrophe exposure in certain areas of the United States (U.S.), such as State Farm and Allstate, who have stopped accepting homeowner insurance applications in California [2, 13]. Rather than stopping insurance altogether, we wish to increase the price of wildfire-prone areas, and propose a new method of rating the risk of wildfires in local zones. Researchers have long attempted to predict wildfire potential and risk across the U.S., namely through the use of data gathered about the climate. For example, a group of people from the National Center for Atmospheric Research in Boulder County, Colorado conducted a study during which they developed a machine learning algorithm to predict the burned area of wildfires across the western U.S. in the summers of 1984-2020 [3]. Using a training set composed of temperature, precipitation, drought, and other factors in the previous winter and spring, the algorithm was able to predict a majority of the wildfire activity [3]. Presently, others continue to monitor and predict wildfire potential across the U.S. For example, the National Interagency Coordination Center produces monthly reports predicting normal, above normal, or below normal wildfire potential for the next four months in different geographic regions across the U.S [8]. The results are based

on temperature, precipitation, drought, and other factors in the month prior to the publication of the report [8]. In addition, Blue Sky Analytics and the United States Geological Survey (USGS) conduct seven-day wildfire potential/risk forecasts [6] [22]. The Blue Sky Analytics' forecast uses satellite imaging and machine learning to produce their forecasts while USGS uses satellite imaging to determine factors such as vegetation and weather to determine their forecasts. Overall, we can see that factors such as temperature, precipitation, wind speed, and previous fires have been used to predict wildfire potential/risk. Therefore, we also seek to use similar factors to assess the potential wildfire risk of different regions across the U.S.

Throughout this report, we will discuss two major approaches to predicting the risk of fires across the US: data analysis for larger scale predictions, and differential equation analysis for finer-grain modeling. In Section 2, we introduce factors like wind capacity factor, maximum temperature, annual precipitation, elevation level, and historical fire occurrences. We use k-means clustering and dynamic mode composition to offer two possible data-driven predictions for fire risk. In the next few sections, we present modeling-based methods using ordinary and partial differential equations. To model how wind flows over irregular topography in localized regions, we present three approaches. Section 3 leverages shallow-water approximations to model wind flow over irregular topography, Section 4 illustrates an exact flow solution, and Section 5 employs a finite element/volume approach.

2. DATA ANALYSIS AND MODELING

2.1. Data Description and Correlation Analysis. In this section, we discuss a data-driven approach to quantifying the risk of wildfires in the United States. We first develop an algorithm to classify land regions according to their risk of a wildfire occurring. This classification is determined by analyzing national US data on four risk factors that have been associated with contributing to wildfires: elevation, temperature, precipitation, and wind capacity factor [8]. We then attempt to predict whether a wildfire will occur in a particular area by using only historical data on the presence of wildfires in that region.

The data used in this section has been collected from various sources. For correlation analysis, we are motivated by the article [4] and use the fire danger data [14], ecoregion boundaries data [11], and elevation data [18] to demonstrate how fire risk may correlate with elevation. In addition, we use daily average temperature data [16] and historical fire events map [17] to inform the correlation between temperature and fire risk. Figure 1 shows that fire risks increases as elevation increases. And Figure 2 indicates that fire tends to occur in high temperature regions.

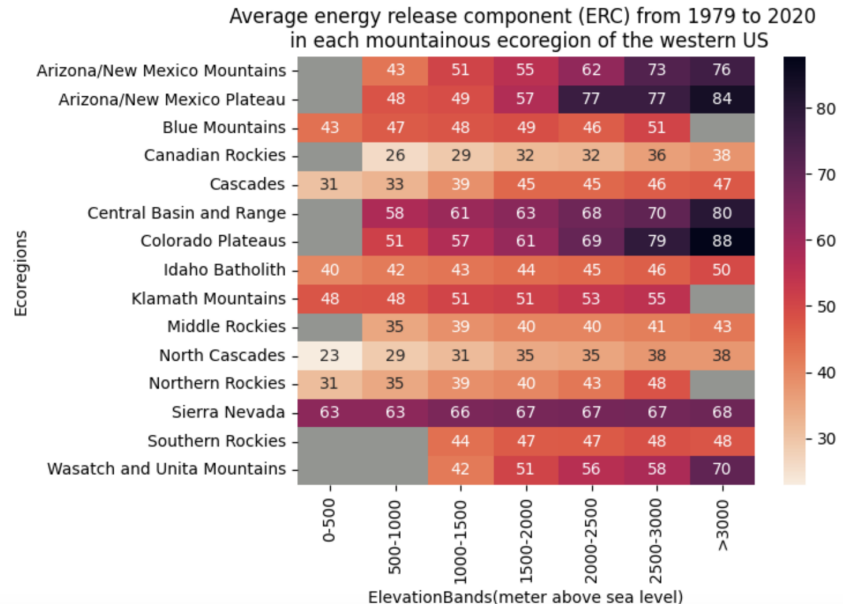


FIGURE 1. Average Energy Release Component from 1979-2020

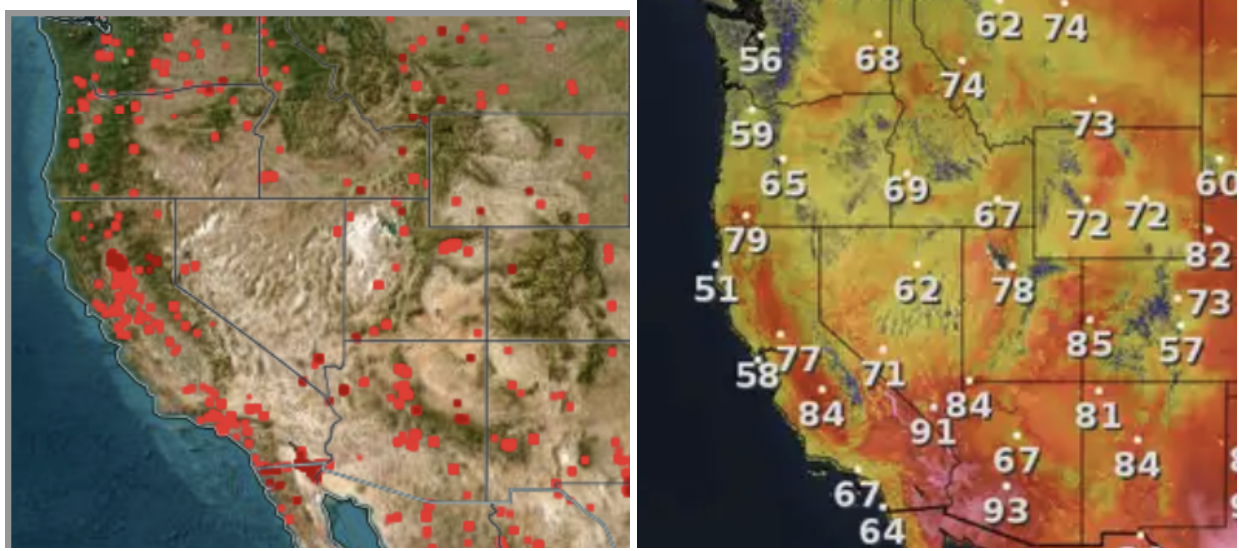


FIGURE 2. Fire events and Average Daily Temperature May 2023.

For our analysis of risk factors, we use the National Renewable Energy Laboratory's data on wind capacity factor in the western United States from 2004-2006 [15]. Wind capacity factor is computed as the ratio of observed wind power to a theoretical maximum power. Additionally, we use the Applied Climate Information Service Web Services to compile data for elevation (ft), maximum annual temperature (F), and total annual precipitation (in) [21]. Each measurement is given for longitude and latitude coordinate pairs. See Figure 3 for visualizations of these four metrics in the southwestern United States. For our analysis of historical fire occurrences, we use measurements of brightness for longitude and latitude coordinate pairs that were collected and published by NASA's Fire Information for Resource Management System [1].

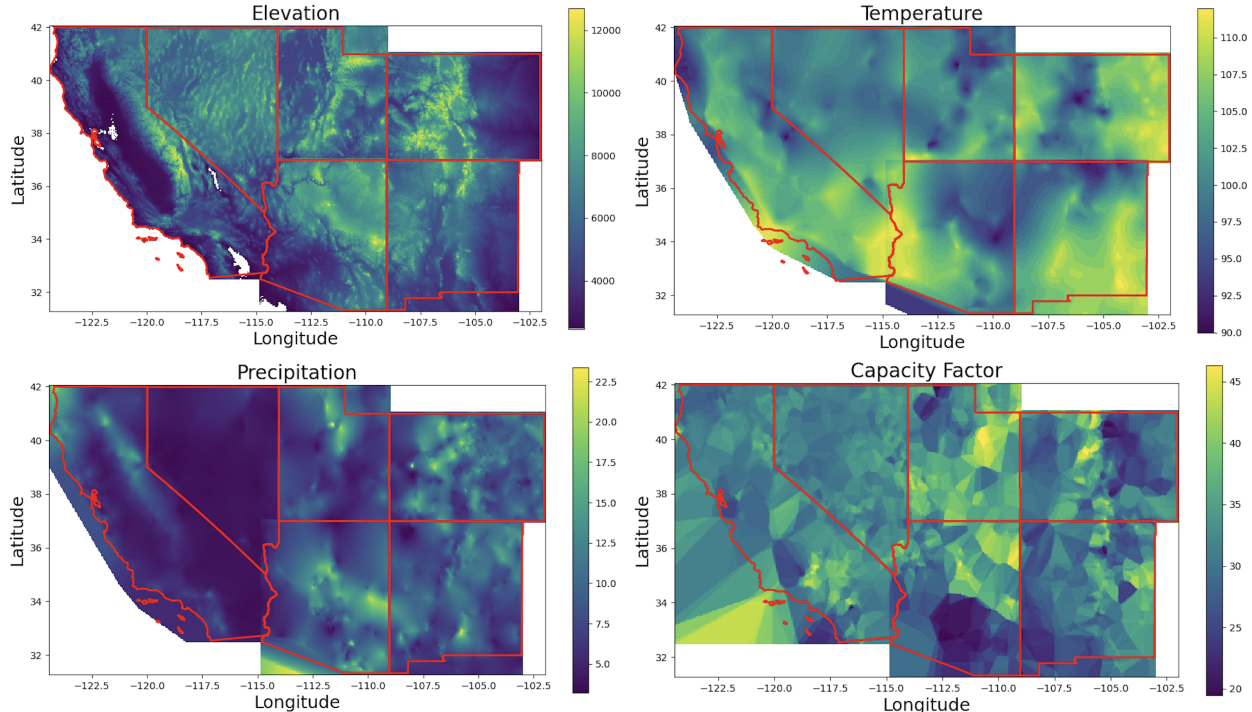


FIGURE 3. Risk factors of wildfires in the southwestern United States.

2.2. K-Means Clustering. Our first algorithm is k -means clustering, which uses measurements of elevation, maximum annual temperature, total annual precipitation, and wind capacity factor. We employ the k -means algorithm to cluster various longitude and latitude coordinate pairs across the southwestern U.S. according to their risk level.

k -means clustering begins by assuming a non-optimal set of k clusters. There are many ways to select the initial cluster centers, and our method uses Lloyd's k -means algorithm, where we randomly select k data points and assign them to be the cluster centers. We then assign each data point to the nearest cluster according to the smallest Euclidean distance from the cluster center. After all the data points have been reassigned, the cluster's center is recalculated as the mean of all the data points currently in the cluster. This cycle is repeated until the difference in the cluster centers of two consecutive iterations is less than 10^{-4} .

For our model, each longitude and latitude coordinate pair is represented by a data point that consists of a value for elevation, temperature, precipitation, and wind capacity factor. After normalizing all the data, we apply k -means to assign each coordinate to one of five clusters. We implement this algorithm over Colorado only (right plot of Figure 4) and over six states in the southwestern US (left plot of Figure 4).

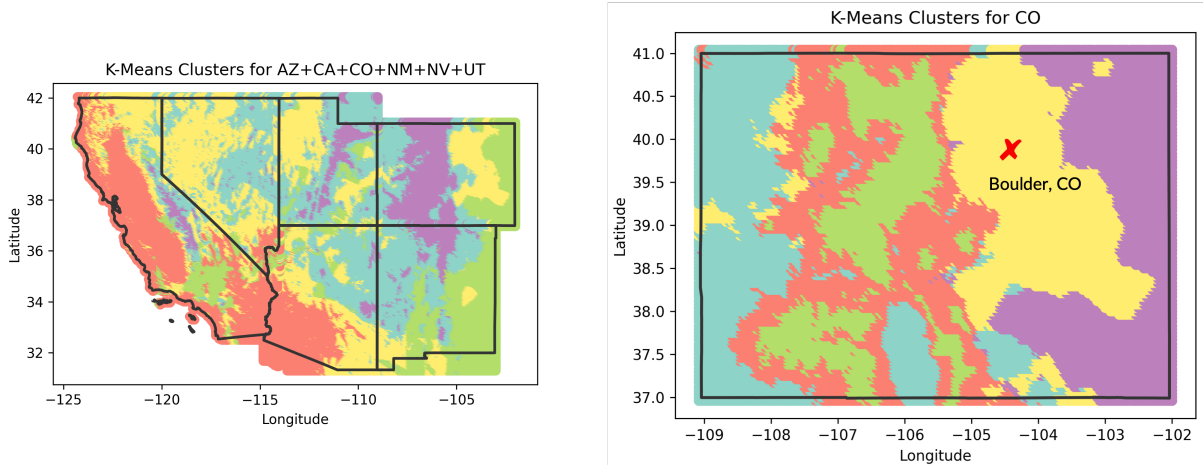


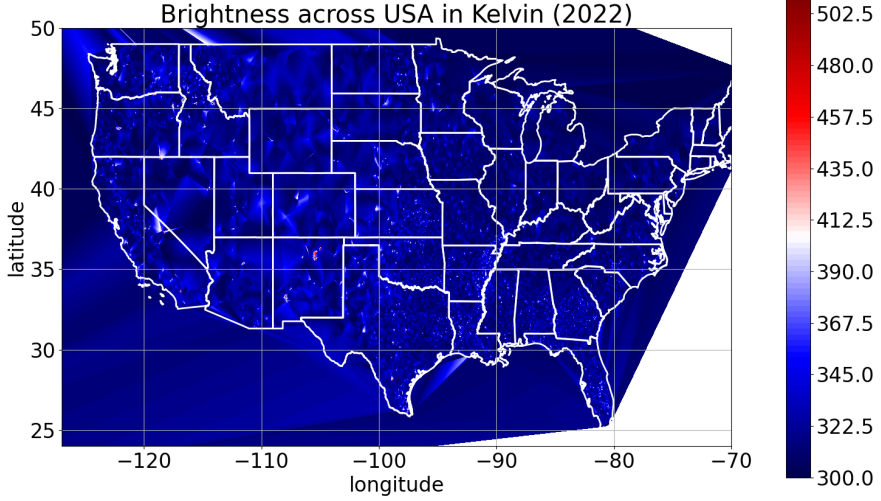
FIGURE 4. K-means clustering for two regions of different geographical scales.

We predict that each resulting cluster has a similar climate, topographic profile, and wind pattern, and thus the land encapsulated by that cluster has a similar level of wildfire risk. With this information, we can identify precisely which areas have the highest risk of fire (based on the temperature, precipitation, elevation, and wind data we used), and hence which regions should be charged more for insurance purposes.

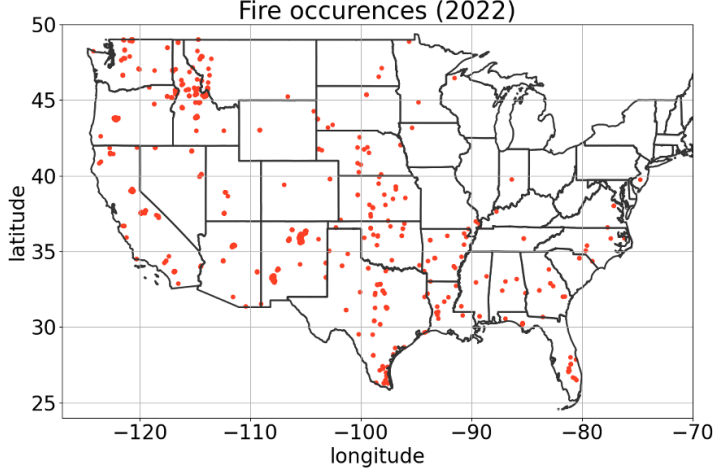
2.3. Dynamic Mode Decomposition Using Historical Fire Data. Besides k -means clustering, another data analysis approach we followed was using Dynamic Mode Decomposition (DMD) on the historical data on fires across the USA. With this approach, and very limited data, we can produce an operator which we can use to predict very broadly where fires will occur one year in the future. We chose DMD to tackle fire location prediction based on historical fire data because it grants us a form of interpretability that is lacking in many standard deep learning approaches. The linear operator produced by the DMD algorithm would grant us eigenvalues and eigenvectors which would correspond to hotspot regions in time.

Below is a sample constructed from the fire dataset which we obtained from NASA. Several thousands of brightness values (measured in degrees Kelvin) were collected over varying longitudes and latitudes for each year from 2000-2022. The size of the historical fire data snapshots were not consistent from year to year. Some years only contained thousands of data points, while others contained tens of thousands. This is conjectured to be a result of increased interest in fire location prediction over the years. Since the time-series snapshots must be of the same size in order to use DMD, this served as a challenge. In order to overcome this, we linearly interpolated the brightness data over a standardized n by n grid of the continental USA. Linearly interpolating over this grid, as well as doing DMD with larger values of n increases the computational cost of our method greatly. We proceeded by interpolating brightness values over a uniform grid with 1600 data

points for each year. Each of these Brightness arrays were considered one standardized sample of data. We treat each of these samples as a time-series snapshot propagated by some linear discrete-time dynamical system.



From this sample, we can see that Brightness is obtained over various (longitude, latitude) pairs.



We assume that a fire has occurred for a given (longitude, latitude) if the brightness for this location is at or above 400 Kelvin.

Since the goal of DMD is to identify the linear matrix operator which propagates a time-series snapshot forward one time-step, this problem formulation is posed as discovering the matrix A in (1). Consider the following linear discrete-time dynamical system

$$(1) \quad Y_{k+1} = A \quad Y_k$$

Based on our context, Y_k represents a current sample of Brightness in Kelvin across the USA that will be propagated forward in time by the matrix A to obtain the future Brightness Y_{k+1} . To construct the *Amatrix* let us introduce the DMD algorithm by initializing our data as snapshot matrices in the following way. Assume we have N samples in time. Then we stack our data in the matrices

$$(2) \quad X_0 = [Y_0 \cdots Y_{N-1}]$$

and

$$(3) \quad X_1 = [Y_1 \cdots Y_N] \quad .$$

Note that N is the number of time-series snapshots and n is the number brightness data points. Now we proceed with the algorithm.

Algorithm 1 Algorithm for the DMD

Data: X_0, X_1

Result: Compute the DMD

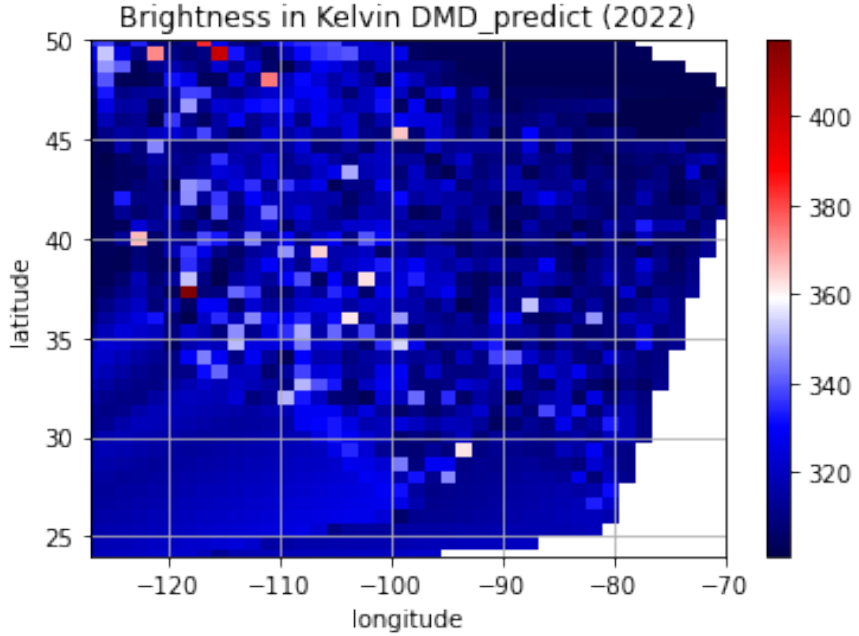
- Compute the SVD of our first matrix $X_0 = U\Sigma V^*$
- Define $A = UX_1V\Sigma^{-1}$
- Compute the eigendecomposition of A
- $AW = W\Lambda$

where W is a matrix of eigenvectors and Λ is a diagonal matrix of eigenvalues λ_i , each λ_i is a DMD eigenvalue

- Compute the DMD eigenmodes, $\Phi = X_1V\Sigma^{-1}W$ Each column of Φ is a DMD mode ϕ_i associated to λ_i
-

From here, we see that we diagonalize the A matrix which was constructed via matrix operations on the Singular Value Decompositions (SVDs) of the X_0 and X_1 snapshot matrices. This gives us the valuable interpretation of the fact that the eigenvalues of A encode for hotspot regions on the map of the USA because every state of our Y_k snapshots gives a brightness value for a specific (longitude, latitude) pair. Hence, with high enough resolution data, we should be able obtain hotspot regions via DMD.

Given the constraints on our data set and dimensionality concerns previously stated, we opted to interpolate a uniformly spaced grid across the USA using only 1600 data points, thus giving us an A matrix of size 1600 by 1600 (n data points give a matrix of size n by n). We were unable to give high-resolution fire location predictions using DMD because the algorithm would take too much time to run on a highly refined grid, and there are plentiful reasons to doubt high resolution predictions from low resolution data. However, given all of the restrictions on our data set, and interpretable method of choice, we are still able to provide a highly generalized data-driven fire prediction as seen below.



We used the first 22 snapshots of Brightness data (from 2000 to 2021) to see if we could predict Brightness values in 2022. From the figure above, it is clear that the Western USA generally will see more fires than the Eastern USA in 2022. Not only is this result corroborated by our other independent analyses, but across the literature as well. Thus, we have shown that DMD can use a very limited and somewhat sparse data set to give general relative predictions of fire occurrences over regions. From this point, there is reason to believe that we could use DMD to get a general sense of where fires are likely to occur using limited data, and then we can use k-means over suspected regions to obtain more refined predictions of high risk fire regions based on a more refined grid.

3. SHALLOW-WATER APPROXIMATIONS FOR MODELING WIND FLOW OVER IRREGULAR TOPOGRAPHY

3.1. Introduction: Shallow-water Equations. We consider the atmosphere flowing over irregular topography over a large spatial domain in 1 dimension. The purpose is to identify topographical features, like mountain shape or distance from a mountain range, that may increase the risk of fire, either by way of faster windspeed or more turbulent wind patterns which may be produced by shocks. Throughout this section, we use windspeed as a proxy for fire risk; faster, more chaotic wind is more conducive to spreading fire.

We make use of the shallow-water equations, which are a simplified 1D version of the Navier-Stokes equations derived by depth-integrating Navier-Stokes [7]. The derivation is highly involved, so we omit it here, but it relies on several assumptions: (1), that the fluid is in hydrostatic balance, i.e. the pressure obeys $p = \rho gh$; (2), that the surface of the fluid is free, which is a standard assumption for the Earth's atmosphere; (3), that the flow reaches a steady-state; and (4), that we may neglect flow in the y -direction. This last condition is acceptable, as our horizontal length scale is much larger than our vertical length scale in this problem. See [9] and [10] for more information and the explicit derivation of these equations, and Figure 5 for a schematic.

The shallow-water equations comprise the momentum equation (4a) and the continuity equation (4b), with initial conditions (4c)

$$(4a) \quad u \frac{du}{dx} + g \frac{dD}{dx} + g \frac{dh}{dx} = 0, \quad x \in (0, L)$$

$$(4b) \quad \frac{d(uD)}{dx} = 0, \quad x \in (0, L)$$

$$(4c) \quad u(0) = u_0, \quad D(0) = d_0$$

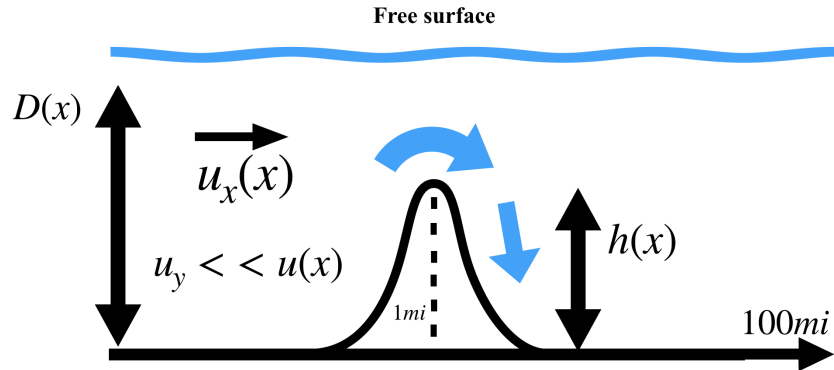


FIGURE 5. Schematic of shallow water approximations. The vertical length scale is negligible relative to the horizontal length scale, and so the velocity in the vertical direction is negligible. This allows for a 1D approximation. The fluid thickness $D(x)$ has a free surface at the top boundary, and is allowed to vary in space. The mountain topography is prescribed as $h(x)$.

Here, $h(x)$ is the 1D topography of the land, $D(x)$ indicates the fluid thickness measured from $y = 0$, and $u(x)$ is the wind velocity in the x -direction; by our assumption that the horizontal length scale (i.e. the size of the domain) is much greater than the vertical length scale, we may assume that the flow is steady and has only a component in the x -direction [7].

In (4a), the three terms are respectively (1) nonlinear advection, (2) the pressure gradient due to changes in fluid thickness, and (3) the component of gravity parallel to the topography. These may be understood by analogy with Navier-Stokes: the advective term is akin to $u \cdot \nabla u$ in the material derivative in the full equations, the pressure gradient term comes from the hydrostatic balance assumption and is analogous to the ∇p in the full equations, and the gravity component term is analogous to including gravity as an external force in the full equations. One may think of equation (4b), the continuity equation, as enforcing a zero-flux condition.

Substituting (4b) into (4a) yields

$$(1 - \text{Fr}^{-2}(x)) \frac{d(D + x)}{dx} = \frac{dh}{dx}$$

where $\text{Fr}^2(x) = \frac{u^2(x)}{gD(x)}$ is the Froude number. This number may be rewritten (using (4b))

$$\text{Fr}^2 = \frac{u \frac{du}{dx}}{\frac{gD}{u} \frac{du}{dx}} = \frac{u \frac{du}{dx}}{-g \frac{dD}{dx}}$$

and so it encodes the ratio of nonlinear advection, $u \frac{du}{dx}$, to the pressure gradient resulting from variable fluid depth, $g \frac{dD}{dx}$. The value of the Froude number gives rise to two qualitatively distinct regimes, supercritical and subcritical flow, based on which of these two terms dominates in the momentum equation. At $\text{Fr} = 1$, the equations have a singularity, which causes a phase transition that we denote a hydraulic jump.

Supercritical flow. This occurs when $\text{Fr} > 1$. Here, advection dominates; fluid particles are accelerated in the same direction as the gravitational force parallel to the topography. This means that as the fluid ascends a mountain, it slows down, then accelerates as it descends the mountain. In the limit $\text{Fr} \gg 1$, (4a) reads $u \frac{du}{dx} = -g \frac{dh}{dx}$, where we see that since u is non-negative, the sign of $\frac{du}{dx}$ is opposite to $\frac{dh}{dx}$, agreeing with the previous observation of decreasing velocity when approaching mountains, and increasing velocity when descending the mountains.

Subcritical flow. This occurs when $\text{Fr} < 1$. Here, the pressure gradient term dominates nonlinear advection. This means that fluid particles accelerate in the direction opposite the gravitational force. In the limit $\text{Fr} \ll 1$, (4a) reads $\frac{d(D+h)}{dx} = 0$, so $D = -h + c$, where c is a constant. Thus, as h increases, D must decrease. Since the velocity is inversely proportional to D by the continuity condition, the velocity increases when ascending a mountain and decreases when descending a mountain.

Hydraulic jumps. So-called hydraulic jumps may occur at the transition from the subcritical to the supercritical regime [19]. From (4b) we have that $u(x)D(x) = u_0 d_0$, where u_0 and d_0 are the initial conditions (4c). Substituting into the Froude number, we have $\text{Fr}^2 = \frac{u^3}{u_0 d_0 g}$. So, $\text{Fr} \sim u^{3/2}$ increases as u increases. Thus, it is possible for a fluid to approach a mountain in subcritical flow (therefore increasing speed), and have Fr to increase enough so that the flow becomes supercritical, hence increasing speed again when descending through the mountains, creating very high wind speeds which may be conducive to greatly increasing overall fire risk. When the flow is supercritical, the speed might increase even more by the presence of a valley or other low altitude areas. See Figure 6 for an illustration of this effect.

To illustrate these different phenomena, the results of the equations with a Gaussian mountain profile for different initial conditions may be found in Figure 7.

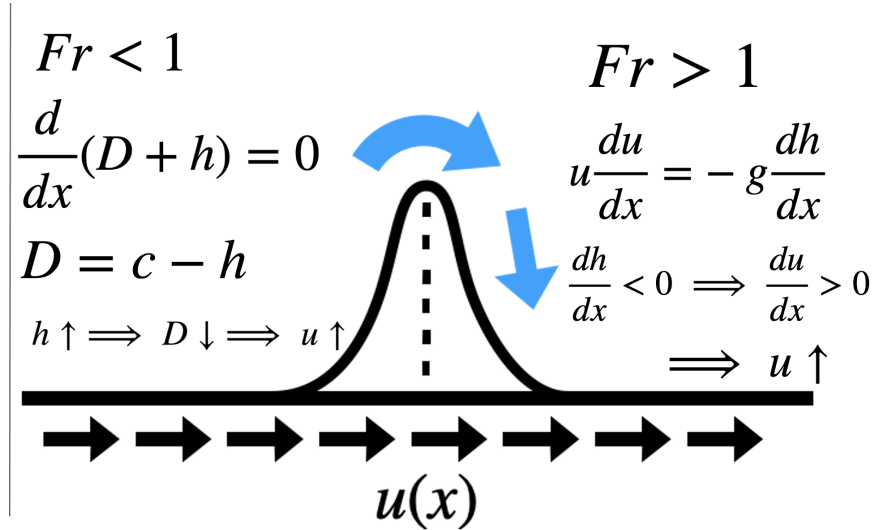


FIGURE 6. Flow approaches a mountain from the left, in the subcritical regime. Since $\text{Fr} < 1$, the advective term in the shallow-water equations is negligible, and windspeed increases as the wind ascends the mountain. This acceleration generates a hydraulic jump; there is a shock, and a phase transition to the $\text{Fr} > 1$ regime. The advective term now dominates the shallow-water equations, and the wind continues to accelerate as it descends the mountain. This leads to potentially extreme wind speeds, and therefore increased fire risk.

3.2. Numerical method. We use the relation $u(x)D(x) = u_0 d_0$ from (4b) to obtain a one-dimensional initial value problem for u , for a given known profile function $h(x)$:

$$(5) \quad \begin{aligned} \frac{du}{dx} \left(u - \frac{gu_0 d_0}{u^2} \right) &= -g \frac{dh}{dx}, \\ u(x_0) &= u_0, \\ D(x_0) &= d_0 \end{aligned}$$

This equation has a discontinuity at $\text{Fr} = 1$, making its direct numerical integration challenging. This corresponds to the hydraulic jump. By integration of separable ODEs we can obtain that for every x , $u(x)$

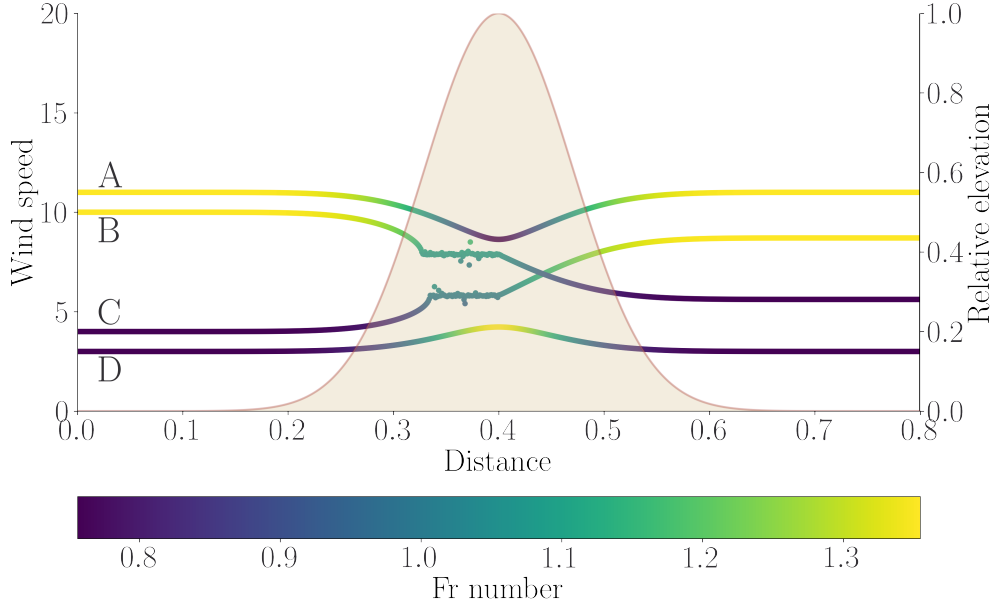


FIGURE 7. Four different behaviors in the shallow-water equation solutions depending on incident wind speed. (A) and (B) correspond to supercritical flow ($\text{Fr} > 1$) initial conditions while (C) and (D) correspond to subcritical flow ($\text{Fr} < 1$) initial conditions. If the wind speed is very large and $\text{Fr} \gg 1$ (A), the mountain temporarily decreases the speed of the wind but the supercritical flow is conserved. If the wind speed is such that $\text{Fr} \sim 1$ (B, C) the mountain can either dramatically reduce or increase the speed, changing the flow to subcritical (B) or supercritical (C) at the other side. Finally, if $\text{Fr} \ll 1$ (D), the mountain will temporarily increase the speed of the wind but the subcritical flow will be preserved

is a root of the polynomial in z

$$(6) \quad p(z; x) = \frac{1}{2}z^3 + \left(gh(x) - gd_0 + \frac{u_0^2}{2} + gh(0) \right) z + gd_0 u_0$$

The phase transition corresponds to different roots “collapsing” into one and becoming complex-valued. This perspective is helpful in verifying that the numerical trajectory found by integrating the PDE is indeed the correct trajectory of u in the presence of the hydraulic jump.

3.3. Predictions arising from shallow-water analysis using elevation data. Based on this analysis, we predict a “highest-risk” topographical scenario based on the assumption (validated by the data analysis in the following sections) that higher windspeed is conducive to increased fire risk. We expect that windspeed may be maximized in the presence of a hydraulic jump, when the wind accelerates rapidly as a result of flow over an irregular surface. Based on the jump mechanism discussed above, we propose that a “worst-case” hydraulic jump may occur at a mountain-valley junction. The wind approaches the mountain at moderate speed, in the subcritical regime, but accelerates as it ascends the mountain. If the Froude number is sufficiently close to 1, this acceleration may induce a shock, and the wind transitions to supercritical; now, it accelerates even more as it descends the mountain. The presence of a valley at the base of the mountain compounds this effect, and the wind continues to accelerate as it descends the valley. Thus, a location at the base of this valley may experience extremely high windspeed, purely as a result of the flow over the topology.

We use elevation data in Colorado to illustrate this effect. Consider a 1D slice of data taken at fixed latitude, running through the Rocky mountains and into the flatlands of Colorado. See Figure 8. All 3 trajectories begin at subcritical windspeeds, and therefore accelerate up the initial peak at longitude -109. Two trajectories sufficiently accelerate such that they transition into the supercritical regime, and continue to accelerate through the descent into the valley at longitude -108. As the trajectories ascend the mountain

range starting at longitude -107, one supercritical trajectory decelerates sufficiently such that it transitions back to the subcritical regime, and decelerates as it moves into the flatlands. However, the other supercritical trajectory does not decelerate enough to transition into the subcritical regime; it continues to accelerate as it moves down the valley. This constitutes a major fire risk, and illustrates the prevalence of fire risk in communities that sit in valleys at the base of mountain ranges.

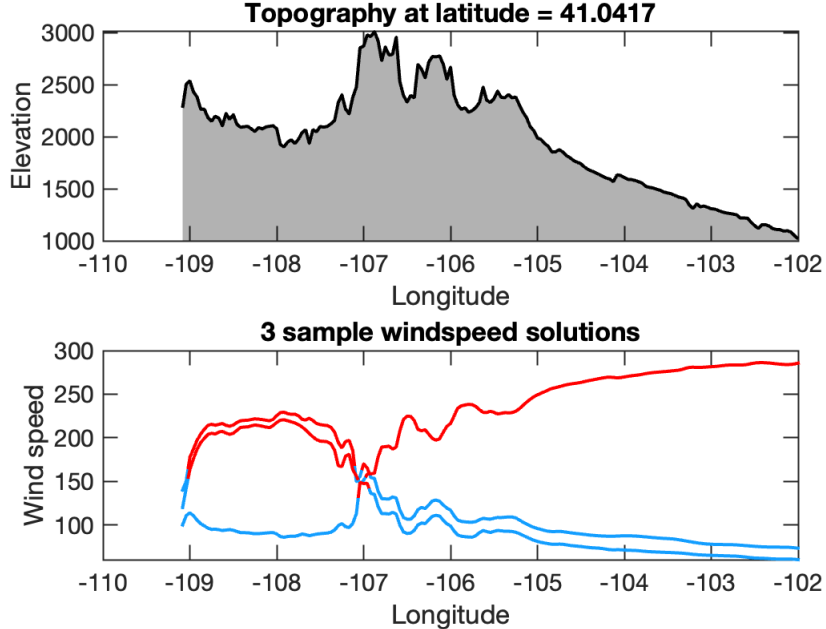


FIGURE 8. Solution to shallow-water equations for wind flowing over real-world topography. In (a), this slice of elevation data is taken at fixed latitude in Colorado, with longitude varying as a domain. In (b), three different incident windspeeds are prescribed. These are $u_0 = \{240, 250, 260\}$. Units of speed are m/s. Supercritical $\text{Fr} > 1$ is plotted in red; subcritical $\text{Fr} < 1$ is plotted in blue. Two wind trajectories undergo a transition from sub- to supercritical flow at the mountain peak around longitude -109, while the lowest initial speed trajectory remains subcritical. Only the highest initial windspeed of $u_0 = 260$ remains supercritical throughout the rest of the topography; the wind accelerates as it flows out of the Rocky Mountains (longitude -107) and into the valley (longitude -105 onward).

4. POTENTIAL FLOW TO MODEL FLOW OVER AN OBSTACLE.

In this section we illustrate an example of an exact flow solution assuming the physics result in potential flow; that is, when the 2D velocity field obeys

$$(7) \quad (u, v) = \nabla \phi$$

for which the velocity potential $\phi(x, y)$ and respective streamfunction $\psi(x, y)$ lead to solving a Laplace equation $\Delta \phi = 0$ with some boundary conditions. In following [23], Section 4, a computational domain for physical (x, y) is formed, then transformed, via

$$(8) \quad X = x + \frac{x}{x^2 + y^2}, \quad Y = y - \frac{y}{x^2 + y^2};$$

then for arbitrary parameters p (“doublet location”) and b (“separation point”), they provide solutions

$$(9) \quad \begin{aligned} \phi(X(x,y), Y(x,y)) &= (X - p) \left[1 + \frac{(p - b)^2}{(X - p)^2 + Y^2} \right] \\ \psi(X(x,y), Y(x,y)) &= Y \left[1 - \frac{(p - b)^2}{(X - p)^2 + Y^2} \right] \end{aligned}$$

We implemented these expressions using standard visualization of functions of two variables in Python, via matplotlib. Two-dimensional rectangular meshes were made for x and y , then in two steps, corresponding (X, Y) were calculated according to Equation 8, followed by the expressions in Equation 9, for various choices of the parameters p and b . Figure 9 illustrates the equipotential lines (left), streamfunctions (center) and velocity magnitude (right) for several choices of p and b as provided in the paper.

This approach (and the handful of additional explicit solutions available via conformal mapping) are useful mainly up to the ability to have “order of magnitude” behaviors to expect. As any pair of choices p, b provide a solution to the semi-infinite flow problem, we hold back from direct numerical comparison or reporting on specific values in these results until p and b can be directly chosen via a careful re-derivation of the potential flow can be decided and a direct relation to physical constants and/or constraints chosen. To illustrate, the right-hand panels of Figure 9 illustrates the magnitude of velocity (arbitrary units); various choices of p , for fixed b , give very different results for the relative jump in wind speed; anywhere from 3 to 27.

We postpone a more careful study to future work and leave this section only as a piece of evidence to validate the physics of downslope flow acceleration, under a slightly different modeling path than other sections in the report.

5. FINITE ELEMENT/VOLUME APPROACHES TO MODELING FLOW

5.1. A finite element approach. To analyze the behavior of downslope winds, we may also look at much larger-scale dynamics. Indeed, consider the following simplified topography:

$$(10) \quad h(x) = \begin{cases} H_m \cos^2 \left(\frac{\pi}{2} \frac{|x - x_c|}{a} \right) & \text{if } \frac{|x - x_c|}{a} \leq 1, \\ 0 & \text{otherwise.} \end{cases}$$

Here, H_m is the height of the mountain, x_c is the center in the horizontal direction, and a is the half-width of the obstacle. Given the stratification of the atmosphere, temperature variations in the vertical direction are not negligible. However, a good approximation to model the flow of air over a mountain is given by the Navier-Stokes equations with a buoyancy term coupling the flow velocity $\mathbf{u} = (u_1, u_2)$ with the temperature T [20]:

$$(11a) \quad \mathbf{u}_t + (\nabla \mathbf{u}) \mathbf{u} = \nu \Delta \mathbf{u} - \nabla p + b(T) \mathbf{k},$$

$$(11b) \quad \nabla \cdot \mathbf{u} = 0,$$

$$(11c) \quad T_t + \mathbf{u} \cdot \nabla T = \kappa \Delta T.$$

In this case, ν and κ are, respectively, the kinematic viscosity and thermal conductivity of air, $b(T)$ is a linear function of temperature, and \mathbf{k} is the unit vector in the vertical direction. The term $b(T)\mathbf{k}$ is usually referred to as the *Boussinesq approximation*.

5.1.1. Numerical methods. The discretization of the full system (11) is known to be a challenging problem. As a first step towards developing a numerical scheme for this problem, we consider first the fluid flow problem given by the Stokes equations:

$$(12a) \quad -\mu \Delta \mathbf{u} + \nabla p = 0,$$

$$(12b) \quad \nabla \cdot \mathbf{u} = 0,$$

where $\mu > 0$ is the dynamic viscosity of air. The computational domain Ω for this problem is shown in Figure 10. In particular, we subdivide the boundary into four parts: $\partial\Omega = \Gamma_1 \cup \Gamma_2 \cup \Gamma_3 \cup \Gamma_4$. Air enters through Γ_1 with horizontal velocity profile, i.e. $\mathbf{u}_{\mathbf{D}} = (u_{max}, 0)$. Then, the air leaves through Γ_4 with no opposed resistance (“do nothing” condition). For the top and bottom boundaries, we choose slip boundary conditions (i.e. $\mathbf{u} \cdot \mathbf{n} = 0$).

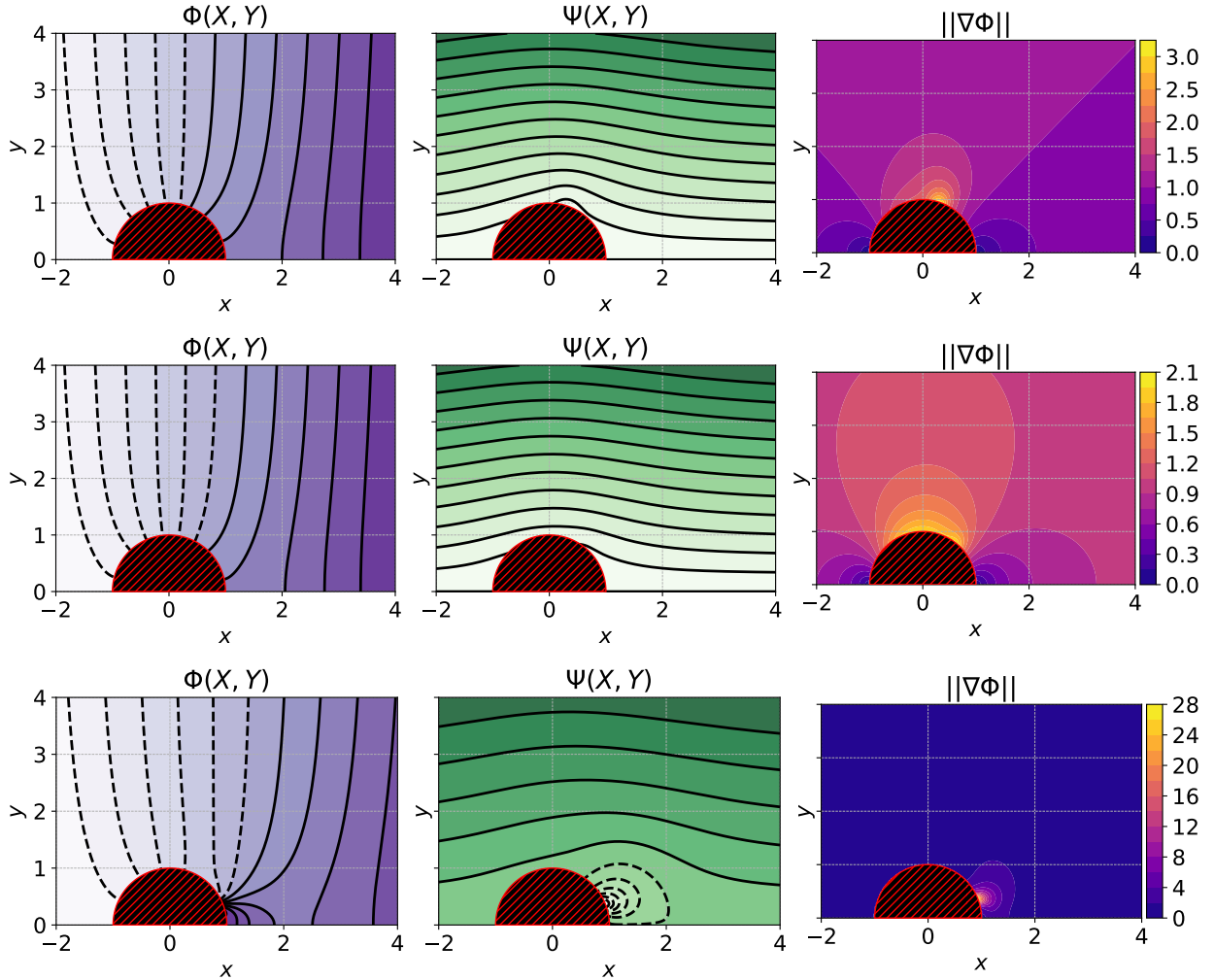


FIGURE 9. Visualizations of exact potential flow solution past an obstruction, following [23], Section 4. Parameters $b = 1$, and going down, $p = 0.6$, $p = 1.2$, $p = 1.8$. The maximum flow speed relative to the upstream flow strongly depends on p , and are numerically approximately 3, 2, and 27, respectively.

Multiple methods are available to solve this equation. Nevertheless, we solve (12) using the finite element method given its flexibility to deal with more irregular domains. We seek a fluid velocity \mathbf{u} and a pressure p such that

$$(13) \quad \mu \int_{\Omega} \nabla \mathbf{u} : \nabla \mathbf{v} - \int_{\Omega} p \operatorname{div}(\mathbf{v}) - \int_{\Omega} q \operatorname{div}(\mathbf{u}) = \alpha \int_{\Gamma_1} (\mathbf{u} \cdot \mathbf{n})(\mathbf{v} \cdot \mathbf{n}),$$

for every test function \mathbf{v} and q . Here, $\alpha > 0$ is a large enough constant to impose the slip boundary condition.

5.1.2. Computational results. In computational terms, we approximate the fluid velocity using piecewise-quadratic continuous polynomials and the pressure using piecewise-linear continuous polynomials (this is the standard Taylor-Hood P_2-P_1 element). The weak formulation (13) is solved using FreeFem++ [12]. We also discretize the domain using 4,634 triangles, as shown in Figure 11. In terms of dimensions, we consider a mountain with height $H_m = 3,280 \text{ ft}$, half-width $a = 5,000 \text{ ft}$, with the center located at $x_c = 25,000 \text{ ft}$. We also consider a width $W = 50,000 \text{ ft}$ (about 9.5 mi), and a height $H = 15,000 \text{ ft}$; the dynamical viscosity of the fluid as $\mu = 1 \text{ ft}^2/\text{s}$ and the boundary penalty term $\alpha = 10^6$.

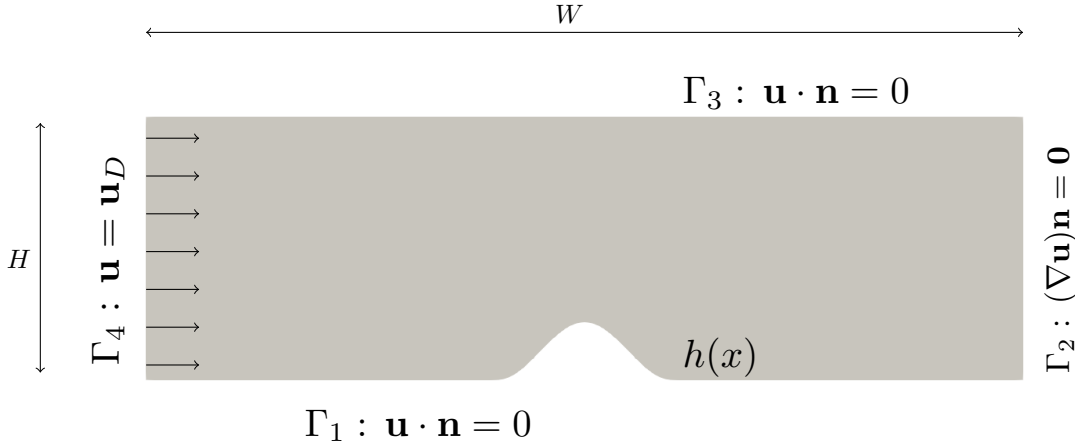


FIGURE 10. Computational domain for the Stokes problem.

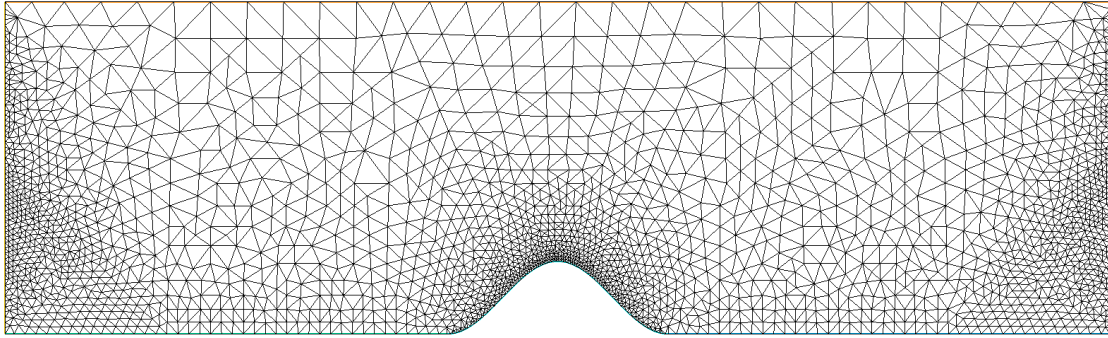


FIGURE 11. Mesh for the computational domain shown in Figure 10.

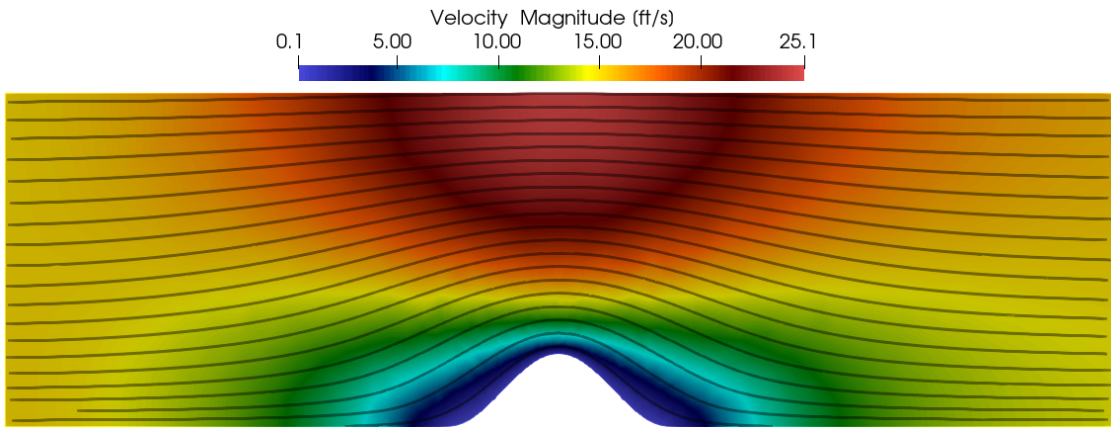


FIGURE 12. Fluid velocity and streamlines of Stokes flow.

In Figures 12 and 13 we show contours of velocity and pressure of air as it flows past the mountain. While this model does not capture the hydraulic jump described in Section 3 and the downslope wind, it does capture the expected behavior for the system (12) and it serves as a prototype of how to solve the system (11). In particular, we observe that the fluid accelerates horizontally as it moves over the mountain. Because the top boundary is modelled as a non-penetrable wall, this is just the Bernoulli effect.

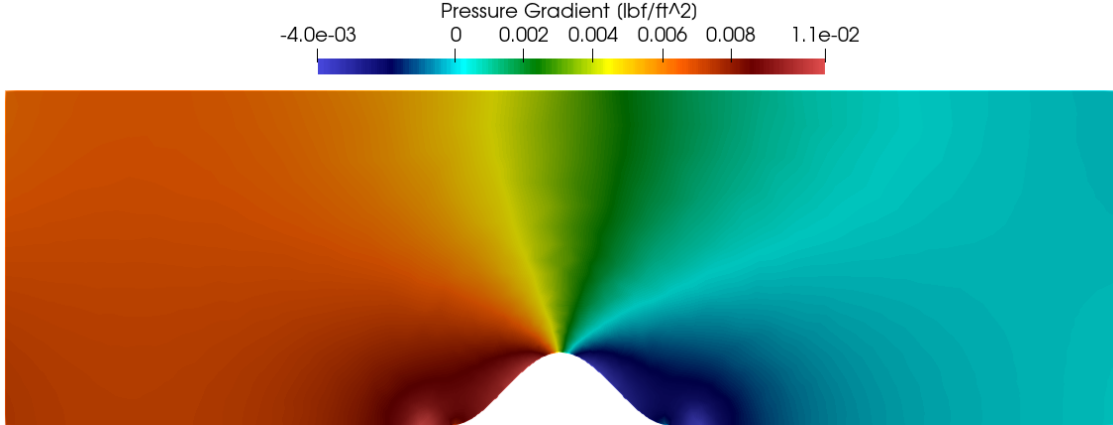


FIGURE 13. Pressure gradient of Stokes flow.

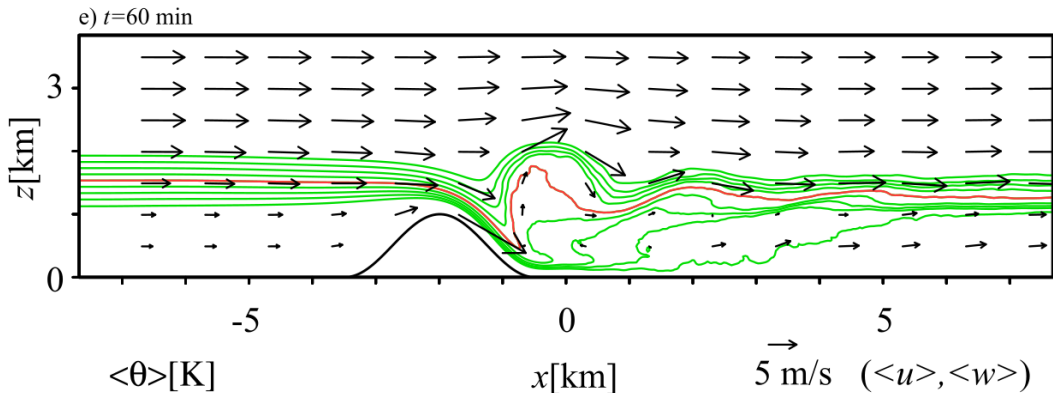


FIGURE 14. Simulation of the full Boussinesq system (11) as shown by Rotundo & Bryan (2018) (see [20]). Observe in the vector field how the numerics capture the downslope wind along the side of the mountain.

5.1.3. Future directions. The results shown in the previous subsection show that it is feasible to solve the full system (11) using the finite element method. On the one hand, as shown in Figure 14, the full Boussinesq system (11) is, indeed, capable of capturing downslope winds. This would allow us to predict, for instance, how fast the wind can get at the bottom of the mountain and how far away from the mountain should a house be placed to avoid these strong winds. On the other hand, to achieve the simulation shown in Figure 14, two things must be addressed.

First, the weak formulation (13) needs to be expanded to include all the terms (including temperature) that are missing from the Boussinesq system (11). The time-dependent terms are particularly important as this flow is rather turbulent ($Re \approx 5,000$, see [20]). Then, to allow more realistic values of viscosity (recall that in the previous example, we considered $\mu = 1 \text{ ft}^2/\text{s}$), the method must be stabilized. This can be achieved by adding stabilizing terms to the weak formulation or by considering a mixed finite element method (such as the one considered in [5]).

5.2. FiPy Simulations. Here we investigate another approach to numerical solution of a wind flow using a prototype geometry and simplified choice of boundary conditions. This section investigates this using the FiPy module in Python, which is a finite volume library to numerically solve partial differential equations.

We investigated two simplified model types and illustrate solutions to show feasibility of the method. For our problem we are using the Poisson equation to model wind flow. Here work off assumptions from a “channel flow,” which could model a wind flow with solid lids on top and bottom and no topography, with

constant pressure gradient $dp/dx = -2$:

$$(14) \quad \Delta u = -2, \quad u(y = -1) = u(y = 1) = 0 \Rightarrow u(y) = 1 - y^2, \quad v \equiv 0.$$

By free association and collectively crossing our fingers, our first study was to seek a flow solution for the horizontal component of velocity in a non-channel computational domain with a similar Poisson problem.

$$(15) \quad \Delta u = -2, \quad u|_{\partial\Omega} = f(s)$$

We importantly note that we posed this problem without concern for whether a corresponding $v(x, y)$ exists or is physically relevant for the problem. This was primarily a first attempt at exploring the capabilities of the FiPy software for solving this class of partial differential equations.

The $f(s)$ represents a parameterized piecewise boundary condition, constant for each edge of the polygon. We have assumed a constant flow of air is coming in from the left and going out at the same speed. In particular, $u = 2$ at the left vertical edge, top horizontal edge and right vertical edge of the hexagon and $u = 0$ on everywhere else on the boundary.

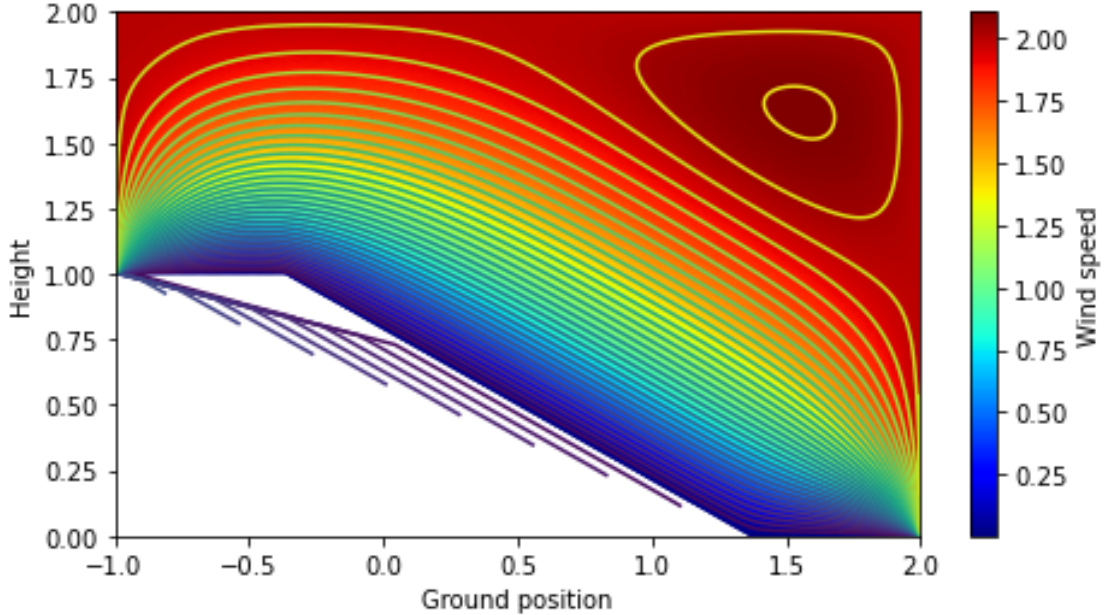


FIGURE 15. Velocity solution $u(x, y)$ of an example non-trivial geometry using FiPy. Dirichlet boundary conditions are imposed on all boundaries; 2 on the sides and top, and 0 at the bottom boundaries.

The second PDE formulation we studied was based on potential flow with Neumann boundary conditions:

$$(16) \quad \Delta\phi = 0; \quad \frac{d\phi}{dn} = g(s)$$

where $g(s)$ represents a parameterized piecewise function on the boundary.

In this case we assumed the slope of the inclined edge to be angle $\pi/6$. The resulting triangular mesh shown has 104720 cells. In this case we have assumed the slope of the inclined edge is $\pi/4$. Our mesh has 104658 cells.

In particular, $\frac{d\phi}{dn} = 2$ at the top horizontal edge of the hexagon and $\frac{d\phi}{dn} = 0$ on everywhere else on the boundary; \mathbf{n} is the unit normal vector. However, since this problem is not uniquely determined (solutions are determined up to constants), the numerical solution was unstable until we fixed the value of ϕ at one point of boundary to prevent the solver from choosing the constant of solution randomly. In Figure 16, we chose the potential to be zero at the very bottom of the inclined edge. We saw sensitive dependence of the details of the flow on the positioning of this point-condition, which suggests pure Neumann conditions are not appropriate for this problem. We leave more detailed study and choice of boundary condition for future work.

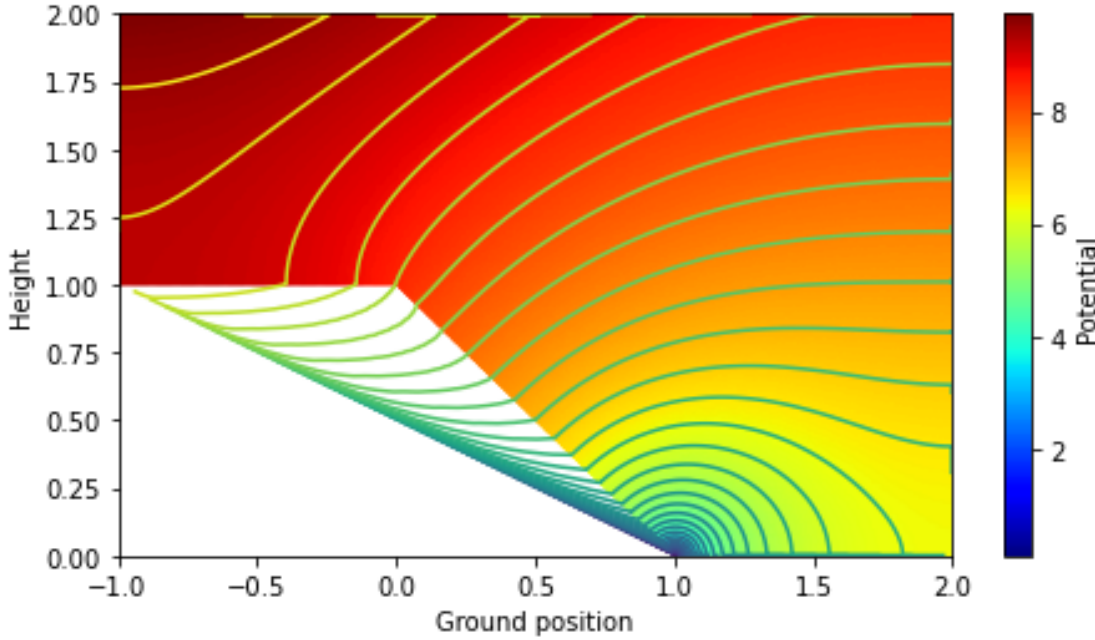


FIGURE 16. Potential flow solution $\phi(x, y)$ of an example non-trivial geometry using FiPy. Zero Neumann boundary conditions are imposed on all boundaries except the top, where the Neumann boundary condition is arbitrarily chosen to be 2. A single function value for $\phi(1, 0)$ is fixed to stabilize the numerical solver. Numerical contours illustrate the boundary conditions are respected.

6. CONCLUSIONS AND FUTURE DIRECTIONS

In this report, we have illustrated methods based in both data analysis and differential equations to predict risk of fire. As higher winds may correlate with increased fire risk, our ODE analysis using shallow-water approximations indicates that regions situated at the base of mountain ranges, or in valleys, may be particularly at risk. Some future directions we envision include:

- **Creating aggregate scores using data-identified risk factors for regions across the US.** By analyzing historical fire data, climate information, land cover patterns, and other relevant variables, it is possible to identify key factors that contribute to fire risk in different regions across the United States. Integrating these factors into a comprehensive scoring system will provide a more accurate and reliable assessment of fire risk, enabling policy makers and land managers to prioritize resources and implement targeted mitigation strategies.
- **Shock resolution.** Simulating the ODE model is complicated due to the shock created at $Fr = 1$, the use of specific algorithms to circumvent this issue would help.
- **Extending the complexity of ODE/PDE models.** By incorporating additional factors or fewer assumptions into our model we can improve the accuracy of fire spread predictions. This includes adding time dependence in the shallow water equations and the full Boussinesq model in the PDE solution.

In conclusion, the future directions outlined above aim to enhance fire risk assessment and management by leveraging data-driven approaches, improving model complexity, incorporating time dependence, resolving shocks, reducing limiting assumptions, and extending existing models.

REFERENCES

- [1] MODIS Collection 6 Hotspot / Active Fire Detections MCD14ML distributed from NASA FIRMS. Available on-line <https://earthdata.nasa.gov/firms.doi:10.5067/FIRMS/MODIS/MCD14ML>.
- [2] Jun 2023.

- [3] Ronnie Abolafia-Rosenzweig, Celin He, and Fei Chen. Winter and spring climate explains a large portion of interannual variability and trend in western u.s. summer fire burned area. *Environmental Research Letters*, 17(5), 2022.
- [4] Mohammad Reza Alizadeh. Elevation-dependent intensification of fire danger in the western united states. *nature*, 2003.
- [5] Javier A Almonacid, Gabriel N Gatica, and Ricardo Oyarzúa. A mixed-primal finite element method for the boussinesq problem with temperature-dependent viscosity. *Calcolo*, 55:1–42, 2018.
- [6] Blue Sky Analytics. Fire predictions. <https://blueskyhq.io/products/fire-predictions>.
- [7] William Blumen. *Atmospheric processes over complex terrain*, volume 23. Springer, 2016.
- [8] National Interagency Fire Center. National significant wildfire potential outlook. https://www.predictiveservices.nifc.gov/outlooks/monthly_seasonal_outlook.pdf.
- [9] Clint Dawson and Christopher M Mirabito. The shallow water equations. *University of Texas, Austin*, 29, 2008.
- [10] Dale R Durran. Downslope winds. *Encyclopedia of atmospheric sciences*, 644:650, 2003.
- [11] EPA. <https://www.epa.gov/eco-research/level-iii-and-iv-ecoregions-continental-united-states>.
- [12] F. Hecht. New development in freefem++. *J. Numer. Math.*, 20(3-4):251–265, 2012.
- [13] Juliana Kim. State farm has stopped accepting homeowner insurance applications in california. *NPR*, May 2023.
- [14] Climatology Lab. <https://www.climatologylab.org/gridmet.html>.
- [15] National Renewable Energy Laboratory. Development of regional wind resource and wind plant output datasets: Final subcontract report, 15 october 2007 – 15 march 2009. <https://www.nrel.gov/grid/western-wind-data.html>.
- [16] NASA. <https://climate.nasa.gov/vital-signs/global-temperature/>.
- [17] nifc. <https://www.nifc.gov/fire-information/maps>.
- [18] NSGS. <https://www.usgs.gov/the-national-map-data-delivery>.
- [19] N Rajaratnam. Hydraulic jumps. In *Advances in hydroscience*, volume 4, pages 197–280. Elsevier, 1967.
- [20] Richard Rotunno and George H Bryan. Numerical simulations of two-layer flow past topography. part i: The leeside hydraulic jump. *Journal of the Atmospheric Sciences*, 75(4):1231–1241, 2018.
- [21] Applied Climate Information Service. https://www.rcc-acis.org/docs_webservices.html.
- [22] United States Geological Survey. Fire danger forecast. <https://firedanger.cr.usgs.gov/viewer/index.html>.
- [23] August Verhoff. Two-dimensional potential flow solutions with separation. *Journal of fluid mechanics*, 657:238–264, 2010.